Journal of Nuclear Materials 389 (2009) 265–278

Contents lists available at ScienceDirect

Journal of Nuclear Materials

journal homepage: www.elsevier.com/locate/jnucmat

Effects of oversized solutes on radiation-induced segregation in austenitic stainless steels

M.J. Hackett [b,*], J.T. Busby [b], M.K. Miller [b], G.S. Was [a]

[a] Nuclear Engineering and Radiological Sciences, University of Michigan, Ann Arbor, MI 48109, USA
[b] Materials Science and Technology Division, Oak Ridge National Laboratory, Oak Ridge, TN 37831, USA

A B S T R A C T

Zirconium or hafnium additions to austenitic stainless steels caused a reduction in grain boundary Cr depletion after proton irradiations for up to 3 dpa at 400 °C and 1 dpa at 500 °C. The predictions of a radiation-induced segregation (RIS) model were also consistent with experiments in showing greater effectiveness of Zr relative to Hf due to a larger binding energy. However, the experiments showed that the effectiveness of the solute additions disappeared above 3 dpa at 400 °C and above 1 dpa at 500 °C. The loss of solute effectiveness with increasing dose is attributed to a reduction in the amount of oversized solute from the matrix due to growth of carbide precipitates. Atom probe tomography measurements indicated a reduction in amount of oversized solute in solution as a function of irradiation dose. The observations were supported by diffusion analysis suggesting that significant solute diffusion by the vacancy flux to precipitate surfaces occurs on the time scales of proton irradiations. With a decrease in available solute in solution, improved agreement between the predictions of the RIS model and measurements were consistent with the solute-vacancy trapping process, as the mechanism for enhanced recombination and suppression of RIS.

1. Introduction

Three hundred series stainless steels have found a broad application in light water reactors for the nuclear industry but have suffered from irradiation-assisted stress corrosion cracking (IASCC) in radiation environments. The depletion of Cr at grain boundaries, a result of radiation-induced segregation (RIS), may be one part of the mechanism for IASCC susceptibility. Mitigating RIS may reduce IASCC susceptibility [1]. The addition of oversized solutes to 316SS has been one method for reducing or eliminating RIS [1–8].

A reduction in RIS by oversized solute atoms is believed to be due to enhanced recombination of defects in the matrix through a solute-vacancy trapping process. Lower defect concentrations mean smaller fluxes to sinks such as grain boundaries, and a reduction in the amount of RIS. The defect microstructure should also be affected, with a reduction in dislocation loop density and/or size.

Shigenaka et al. [5] irradiated 316L stainless steel containing Zr with 400 keV He^+ ions at 500 °C to doses up to 3.4 dpa to show a gradual reduction in RIS with increasing Zr concentration until RIS was eliminated by 0.41 wt% Zr. Sakaguchi et al. [4] made additions of 0.5 at.% of Ti, Nb, Hf or Zr to 316SS and observed that Zr and Hf showed the largest reduction in RIS. High purity 316SS containing Hf that was p^+ irradiated at 400 °C showed a substantial reduction in Cr depletion at 2.5 dpa, though the effect mostly disappeared by 5 dpa [1,9]. Meanwhile, the total dislocation loop line length was reduced substantially, and no significant void swelling was observed, confirming that Hf addition had enhanced the recombination of defects in the matrix.

However, data in the literature do show some confusing trends. Recent work involving neutron irradiations suggested that even with Zr additions, significant RIS still developed between 430 and 444 °C, even at a low dose of 0.38 dpa [10], where RIS should have been low with or without solute additions. A study on a 316SS that was p^+ irradiated at 400 °C to 1.0 dpa concluded that there was no observed benefit of Zr on Cr depletion, although there was a reduction in the enrichment of Ni [2]. On the other hand, electron irradiations up to 10.8 dpa by Kato et al. [6] at 500 °C showed nearly complete suppression of RIS for a 316SS with Hf or Zr additions, whereas Kasahara et al. [5] measured just a partial reduction in RIS for a 316SS containing 0.2 at.% Zr electron irradiated at 500 °C to 10 dpa.

Many of the results in the literature are conflicting or lead to different conclusions regarding the effects of oversized solutes on RIS. The primary objective of this work is to establish the mechanism by which oversized solute atoms reduce RIS in stainless steel. This is accomplished by determining: (1) the effect of a range of solute concentrations, solute types, and irradiation temperatures, and irradiation dose on Cr depletion, (2) the effect of oversized

* Corresponding author. Present address: Knolls Atomic Power Laboratory, P.O. Box 1072, Schenectady, NY 12309, USA.
E-mail address: mjhacket@umich.edu (M.J. Hackett).

0022-3115/$ - see front matter © 2009 Elsevier B.V. All rights reserved.
doi:10.1016/j.jnucmat.2009.02.010

solutes on loop microstructure, and (3) the ability of a solute-vacancy trapping mechanism to accurately simulate experimental RIS measurements of oversized solutes.

2. Experimental procedure

Six different stainless steel alloys were used in this study and were divided into two sets. Each set has a reference alloy, and the oversized solute alloys contained 0.19 or 0.28 at.% Zr or, with 0.05 or 0.37 at.% Hf. The concentration of the oversized solute was varied to study the effect of both solute concentration as well as the differences of solute type on RIS. The compositions of these alloys are given in Table 1. Both the LoZr and HiZr were fabricated by MetalMen, Inc., whereas the remaining alloys were from General Electric Global Research Center. Thermomechanical processing involved a solution anneal at 1200 °C for 24 h followed by 50–66% cold work with subsequent recrystallization heat treatments at 850–1000 °C for 1–2 h to obtain similar grain sizes for all of the alloys. Average grain sizes for the alloys ranged from 13 to 27 μm, and no effect of differences in grain size on RIS is expected.

Sample bars with dimensions of $2 \times 2 \times 20$ mm were mechanically wet polished using SiC paper (grit 320–4000), followed by a 30-s electropolish in a 10% perchloric acid and 90% methanol solution at −55 °C and ~32 V. The purpose of the electropolish was to remove any remaining surface damage layer due to mechanical polishing.

Irradiations were conducted with either 2 or 3.2 MeV protons in the Michigan Ion Beam Laboratory, with irradiation current adjusted to achieve the same dose rate of $\sim 1.0 \times 10^{-5}$ dpa/s for both proton energies in the uniform damage region from 5 to 20 μm. Sample temperature was maintained at 400 ± 10 °C using a liquid indium layer underneath the samples for heat transfer to dissipate heat from the proton beam and maintain a uniform temperature across the sample stage. Surface temperature was monitored using an IRCON Stinger thermal imaging system. Irradiations were performed to doses of 3, 7 and 10 dpa at 400 °C and 1 and 3 dpa at 500 °C. Additional details on the proton irradiation technique can be found in Ref. [11].

Microchemistry measurements were made with a CM200/FEG at Oak Ridge National Laboratory (ORNL) equipped with an energy-dispersive X-ray spectrometer (STEM/EDS) with a probe size of ~1.2 nm diameter (full-width, half-maximum) at 200 kV. Measurements were performed after aligning the grain boundaries to be 'edge-on' to the incident electron probe to maximize beam exposure of the grain boundary. Grain boundaries were measured in thin areas to minimize beam broadening. Two or more grain boundaries for each alloy condition were measured, with six profile measurements across each boundary. Composition measurements for all boundaries of a sample were averaged together to determine the average depletion or enrichment for each element at the grain boundary due to irradiation. The amount of segregation was taken as the difference between the grain boundary (GB) measurement and the measurement of the bulk composition taken away from the boundary.

Microchemistry data was collected and analyzed using EMiSPEC ESVision software. Intensity data was converted to atomic percent by calculating k-factors based on matrix values. k-Factors relating the measured X-ray intensity to the local chemical composition were determined by the method in Ref. [12]. Multiple area scans measuring the matrix bulk composition were averaged to determine the k-factors.

The microstructure results were obtained on a JEOL 2010F TEM at the University of Michigan. Dislocation imaging was performed using the relrod technique to image only Frank loops which are radiation-produced dislocations that cause hardening. Frank loops are faulted loops with $\boldsymbol{b} = a_0/3$ [1 1 1] and can be imaged by tilting off the [0 1 1] zone axis and inserting the objective aperture around the relrod streaks that form along the $\boldsymbol{g} = 113$ reflection between the $\boldsymbol{g} = 200$ and $\boldsymbol{g} = 111$ reflections [13]. Dislocation loops from the images were measured and counted for loop microstructure results. Sample thickness was measured from the zero energy-loss peak using electron energy loss spectroscopy (EELS).

In all of the oversized solute alloys, secondary precipitate phases were identified in the matrix using both SEM and TEM. Determination of the precipitate phases in the oversized solute alloys was done by X-ray diffraction (XRD) using a Bruker D8 Discover GADDS and a Rigaku Dmax B. Multiple scans were made of each of the six alloys, including all oversized solute alloys and the reference alloys, to ensure the accuracy of results. ZrC was detected in the LoZr and HiZr alloys and HfC was identified in the HiHf alloy only. No secondary phases were observed in the diffraction pattern for LoHf, even though precipitates were visible in the microstructure, because the volume fraction was too low. Only the austenite phase was identified in either of the reference alloys.

Atom probe tomography (APT) was performed at ORNL with an Imago Scientific Local Electrode Atom Probe for the detection of oversized solute remaining in solution. APT combines time-of-flight spectroscopy and field ion microscopy (FIM) to create three-dimensional composition maps with atomic resolution. Electropolishing was used for the preparation of unirradiated specimens, whereas irradiated specimens were fabricated from thin TEM foils using the sample lift-out method with a FEI Nova 200 Dual-Beam Focused Ion Beam (FIB). The final steps of tip fabrication used low currents (0.1 nA) to isolate beam damage to a few monolayers of the sample tip, and these layers would be evaporated prior the start of data collection in LEAP. Each of the oversized solute alloys was analyzed in the unirradiated condition with additional analysis performed on the LoZr, HiZr and HiHf alloys irradiated at 400 °C. A detailed review of the specimen preparation method is covered by Miller et al. in Refs. [11,14]. A specimen temperature of 60 K, a pulse repetition rate of 200 kHz and a pulse ratio of 0.2 were used for these analyses.

Error analysis of the microchemistry and microstructure measurements used one standard deviation of the measurements for each alloy condition. Grain boundary segregation values represent the difference between matrix and grain boundary measurements, so a propagation of error is required to determine the standard deviation of segregation.

Table 1
Summary of bulk alloy compositions (wt%) determined by chemical analysis.

Alloy	Fe	Cr	Ni	Mo	C	Mn	Si	P	S	Zr	Hf
Sample composition (wt%)											
316-Ref-Zr	Bal.	69.75	15.26	12.68	0.09	0.23	1.22	0.75	0.009	<0.01	<0.01
316+LoZr	Bal.	69.25	15.34	12.79	0.10	0.23	1.31	0.75	<0.005	0.038	–
316+HiZr	Bal.	69.82	14.83	12.73	0.10	0.23	1.19	0.79	<0.005	0.038	–
316-Ref-Hf	Bal.	65.16	18.97	13.19	1.30	0.10	1.02	0.24	0.010	<0.01	<0.01
316+LoHf	Bal.	65.68	18.73	12.81	1.27	0.12	1.03	0.28	0.012	–	0.05
316+HiHf	Bal.	65.44	18.45	13.06	1.28	0.13	1.04	0.20	0.012	–	0.37

3. Results

This section presents RIS, loop microstructure and precipitate microstructure characterization resulting from proton irradiation at 400 and 500 °C.

3.1. Grain boundary segregation

For every alloy condition measured, there is depletion of Fe and Cr and enrichment of Ni. Changes in Cr depletion for the oversized solute alloys are mirrored by similar changes in Ni enrichment. In reporting the RIS data, however, all of the measured segregation data are presented. For the +Zr alloys (Ref-Zr, LoZr and HiZr), this includes Fe, Cr, Ni, Mn, Si and Zr. For the +Hf alloys (Ref-Hf, LoHf and HiHf), the measured segregation data include Fe, Cr, Ni, Mn, Mo and Si. However, since the objective is to focus on the effects of Zr and Hf on segregation behavior, results will focus on changes in segregation of Cr as an indicator of the effectiveness of the oversized solutes in affecting RIS.

Segregation of the minor elements is not significant for all cases examined. Mn depletion is always less than 1 at.% for any of the +Zr or +Hf alloys at either 400 or 500 °C. Mo depletion is likewise less than 1 at.% for all conditions in the +Hf alloys; for the +Zr alloys, no Mo data is reported because the alloy concentration is too low to be measured. Si enrichment ranges from 0.04 to 1.13 at.% for the +Hf alloys and from 0.48 to 3.43 at.% for the +Zr alloys. The higher amount of Si enrichment in the +Zr alloys relative to the +Hf alloys is due to a bulk Si level that is three times more than the +Hf alloys. Zr is detected at the grain boundary in some spectra, with increases in the grain boundary concentration up to 0.78 at.% for both 400 and 500 °C measurements of the +Zr alloys. With an estimated minimum detectability of ~0.4 at.%, measurements below this concentration were considered not measurable. For the +Hf alloys, no Hf is detected in any of the RIS profiles, whether at the grain boundary or in the matrix, where the detectability limit is estimated to be ~1.7 at.% [11], so no Hf data is reported. Based on these results, the tracking of Cr segregation as an indicator of solute effectiveness on RIS is reasonable.

3.1.1. RIS at 400 °C

All RIS measurements for the +Zr and +Hf alloys irradiated at 400 °C are given in Tables 2 and 3, respectively. The results are normalized to Fe + Cr + Ni + Mn + Si + Zr = 1 for the +Zr alloys and normalized to Fe + Cr + Ni + Mn + Mo + Si = 1 for the +Hf alloys. The tables present both the average grain boundary concentrations and average matrix concentrations, with accompanying uncertainties. Included are the total number of RIS profile measurements that were made and the number of different grain boundaries that were measured. In addition, the tables provide segregation data renormalized to Fe + Cr + Ni = 1 in order to compare the experimental segregation results to theoretical model results later on. All RIS measurements were performed with the techniques described in Section 2.

Measured Cr concentration profiles for the +Zr alloys at doses of 3, 7 and 10 dpa are shown in Fig. 1(a). Similar profiles for the +Hf alloys are shown in Fig. 1(b). At the lowest dose of 3 dpa, there is a large difference in the amount of Cr depletion between Ref-Zr and both LoZr and HiZr. Ref-Zr shows Cr depletion of 6.8 at.% compared to just 1.7 at.% for LoZr and 2.4 at.% for HiZr. The difference between Ref-Zr from LoZr and HiZr is 5 at.%, whereas the difference between LoZr and HiZr is less than the experimental uncertainty of their measurements. The results at 3 dpa show that Zr addition results in significantly less Cr depletion.

By 7 dpa, there is no measurable difference in Cr depletion between Ref-Zr and LoZr and a small difference from HiZr. LoZr has a similar amount of Cr depletion, at 6.1 at.%, as Ref-Zr, with 6.8 at.%. HiZr is still about 2 at.% less than Ref-Zr, at 4.7 at.% Cr depletion. Although RIS in Ref-Zr is not measured at 10 dpa, the results are expected to be similar to those at 7 dpa since Cr depletion did not change substantially between 3 and 7 dpa for this alloy. Likewise, RIS in LoZr and HiZr did not change beyond their measurement uncertainty from 7 to 10 dpa, with Cr depletion of 5.6 at.% for LoZr and 3.5 at.% for HiZr at 10 dpa. The high dose results show that only the HiZr still measures a reduction in Cr depletion.

For the +Hf alloys at 3 dpa, the amount of segregation decreases with increasing Hf concentration, where Ref-Hf has the most segregation and HiHf has the least segregation. Cr depletion for Ref-Hf was 7.6 at.% compared to 6.4 at.% for LoHf and 4.9 at.% for HiHf. The difference between Ref-Hf and LoHf is less than the range of their measurement error. Even for HiHf, Cr depletion is only about 3 at.% lower than Ref-Hf.

At 7 dpa, however, segregation behavior is not the same. HiHf has the most segregation, with 8.6 at.% Cr depletion, and LoHf has the least segregation, with 5.6 at.% Cr depletion. Segregation for Ref-Hf is somewhere in between, with 7.5 at.% Cr depletion. The results at 7 dpa, where HiHf has the most segregation, is inconsistent

Table 2
Grain boundary concentration measurements for the +Zr alloys irradiated with protons at 400 °C to doses of 3, 7 and 10 dpa.

Alloy	Dose (dpa)	# of GB's	# of profile measured		Measured concentration (at.%), normalized to 1						Segregation (at.%), renormalized		
					Fe	Cr	Ni	Mn	Si	Zr	Fe	Cr	Ni
Ref-Zr	3	2	15	GB	53.4 ± 2.8	8.5 ± 0.5	34.0 ± 4.3	0.58 ± 0.19	3.44 ± 0.74	–	−15.5 ± 3.1	−6.8 ± 0.6	22.3 ± 4.7
				Matrix	69.7 ± 1.3	15.4 ± 0.4	12.9 ± 1.8	1.24 ± 0.24	0.78 ± 0.23	–			
	7	2	6	GB	55.3 ± 0.6	9.2 ± 0.2	30.8 ± 0.6	0.53 ± 0.04	4.19 ± 0.09	–	−13.2 ± 0.9	−6.1 ± 0.6	19.3 ± 0.8
				Matrix	69.8 ± 0.6	15.4 ± 0.6	12.8 ± 0.5	1.24 ± 0.15	0.76 ± 0.09	–			
LoZr	3	2	15	GB	66.5 ± 0.4	13.7 ± 0.3	15.5 ± 0.3	1.52 ± 0.19	2.57 ± 0.16	NM	−1.6 ± 0.5	−1.4 ± 0.3	3.1 ± 0.3
				Matrix	69.5 ± 0.1	15.4 ± 0.1	12.8 ± 0.1	1.32 ± 0.06	0.75 ± 0.03	NM			
	7	2	7	GB	62.4 ± 0.6	9.3 ± 0.7	25.7 ± 0.6	0.52 ± 0.22	1.86 ± 0.14	NM	−7.0 ± 0.9	−6.2 ± 0.8	13.2 ± 1.0
				Matrix	69.4 ± 0.7	15.4 ± 0.3	12.9 ± 0.8	1.37 ± 0.26	0.76 ± 0.10	NM			
	10	3	14	GB	62.9 ± 3.2	9.6 ± 0.6	22.1 ± 2.0	1.18 ± 0.39	3.13 ± 0.95	0.98 ± 0.43	−4.6 ± 3.3	−5.6 ± 0.7	10.2 ± 2.2
				Matrix	69.4 ± 0.9	15.4 ± 0.4	12.9 ± 0.9	1.33 ± 0.15	0.86 ± 0.38	NM			
HiZr	3	4	13	GB	67.6 ± 0.5	12.4 ± 0.3	16.7 ± 0.7	0.89 ± 0.16	1.58 ± 0.07	0.83 ± 0.09	−1.8 ± 0.8	−2.4 ± 0.5	4.2 ± 0.9
				Matrix	69.9 ± 0.7	14.9 ± 0.4	12.8 ± 0.8	1.24 ± 0.19	0.83 ± 0.05	NM			
	7	4	27	GB	64.5 ± 1.7	10.2 ± 0.4	21.9 ± 1.8	0.73 ± 0.11	2.23 ± 0.28	0.43 ± 0.07	−4.9 ± 1.8	−4.7 ± 0.6	9.6 ± 1.9
				Matrix	70.0 ± 0.6	14.9 ± 0.4	12.8 ± 0.5	1.21 ± 0.16	0.82 ± 0.15	NM			
	10	2	18	GB	66.7 ± 1.8	11.4 ± 0.7	19.4 ± 1.9	0.65 ± 0.20	1.58 ± .027	NM	−3.3 ± 2.1	−3.5 ± 0.8	6.8 ± 2.3
				Matrix	70.0 ± 1.1	14.9 ± 0.7	12.8 ± 1.2	1.20 ± 0.19	0.80 ± 0.15	NM			

Uncertainties represent one standard deviation of the measured data.
NM: Not Measurable.

Table 3
Grain boundary concentration measurements for the +Hf alloys irradiated with protons at 400 °C to doses of 3, 7 and 10 dpa.

Alloy	Dose (dpa)	# of GB's	# of profile measured		Measured concentration (at.%), normalized to 1						Segregation (at.%), renormalized		
					Fe	Cr	Ni	Mn	Mo	Si	Fe	Cr	Ni
Ref-Hf	3	4	21	GB	61.2 ± 1.8	11.5 ± 0.6	24.4 ± 2.1	0.61 ± 0.20	1.19 ± 0.10	1.17 ± 0.13	−3.6 ± 2.0	−7.8 ± 0.9	11.4 ± 2.2
				Matrix	64.9 ± 0.8	19.1 ± 0.6	13.3 ± 0.8	1.09 ± 0.17	1.33 ± 0.31	0.27 ± 0.09			
	7	4	12	GB	59.8 ± 2.6	11.7 ± 0.6	26.6 ± 2.7	0.50 ± 0.17	0.66 ± 0.18	0.86 ± 0.33	−5.7 ± 2.7	−7.7 ± 0.8	13.4 ± 2.7
				Matrix	64.9 ± 0.7	19.1 ± 0.5	13.3 ± 0.5	1.06 ± 0.30	1.37 ± 0.21	0.27 ± 0.11			
	10	2	12	GB	61.2 ± 0.5	12.2 ± 0.2	25.1 ± 0.6	0.44 ± 0.18	0.45 ± 0.01	0.63 ± 0.01	−4.6 ± 0.7	−7.2 ± 0.4	11.8 ± 0.7
				Matrix	64.9 ± 0.5	19.1 ± 0.3	13.3 ± 0.4	1.06 ± 0.21	1.33 ± 0.16	0.27 ± 0.10			
LoHf	3	2	15	GB	65.0 ± 1.5	12.3 ± 0.7	21.1 ± 1.9	0.43 ± 0.18	0.74 ± 0.29	0.42 ± 0.17	−1.5 ± 1.7	−6.7 ± 1.0	8.2 ± 2.0
				Matrix	65.8 ± 0.8	18.8 ± 0.8	12.9 ± 0.7	1.05 ± 0.14	1.29 ± 0.15	0.28 ± 0.03			
	7	2	8	GB	63.4 ± 0.3	13.2 ± 0.7	21.6 ± 1.2	0.53 ± 0.13	0.82 ± 0.3	0.54 ± 0.04	−2.9 ± 0.8	−5.8 ± 0.9	8.7 ± 1.3
				Matrix	65.7 ± 0.7	18.8 ± 0.6	12.9 ± 0.5	1.05 ± 0.17	1.28 ± 0.10	0.28 ± 0.03			
	10	2	10	GB	60.9 ± 2.2	11.1 ± 1.2	25.2 ± 2.7	0.55 ± 0.25	0.69 ± 0.31	1.46 ± 0.32	−4.9 ± 2.5	−7.8 ± 1.4	12.7 ± 3.0
				Matrix	65.7 ± 1.2	18.7 ± 0.6	12.9 ± 1.2	1.06 ± 0.30	1.32 ± 0.38	0.34 ± 0.19			
HiHf	3	4	28	GB	65.7 ± 0.9	13.5 ± 0.9	18.7 ± 1.5	0.66 ± 0.19	0.99 ± 0.12	0.42 ± 0.04	−0.5 ± 1.1	−5.2 ± 1.2	5.7 ± 1.6
				Matrix	65.8 ± 0.7	18.4 ± 0.7	13.1 ± 0.6	1.06 ± 0.12	1.41 ± 0.14	0.22 ± 0.02			
	7	4	20	GB	61.9 ± 1.5	9.9 ± 0.5	26.0 ± 1.9	0.59 ± 0.08	0.75 ± 0.07	0.41 ± 0.05	−4.5 ± 1.5	−8.9 ± 0.5	13.4 ± 1.9
				Matrix	65.7 ± 0.1	18.5 ± 0.3	13.2 ± 0.3	1.06 ± 0.03	1.32 ± 0.02	0.21 ± 0.02			
	10	2	12	GB	64.2 ± 0.6	12.1 ± 0.8	22.0 ± 1.4	0.51 ± 0.12	0.84 ± 0.07	0.38 ± 0.03	−2.2 ± 0.9	−6.7 ± 0.9	8.9 ± 1.5
				Matrix	65.7 ± 0.6	18.5 ± 0.5	13.1 ± 0.6	1.06 ± 0.14	1.32 ± 0.20	0.22 ± 0.05			

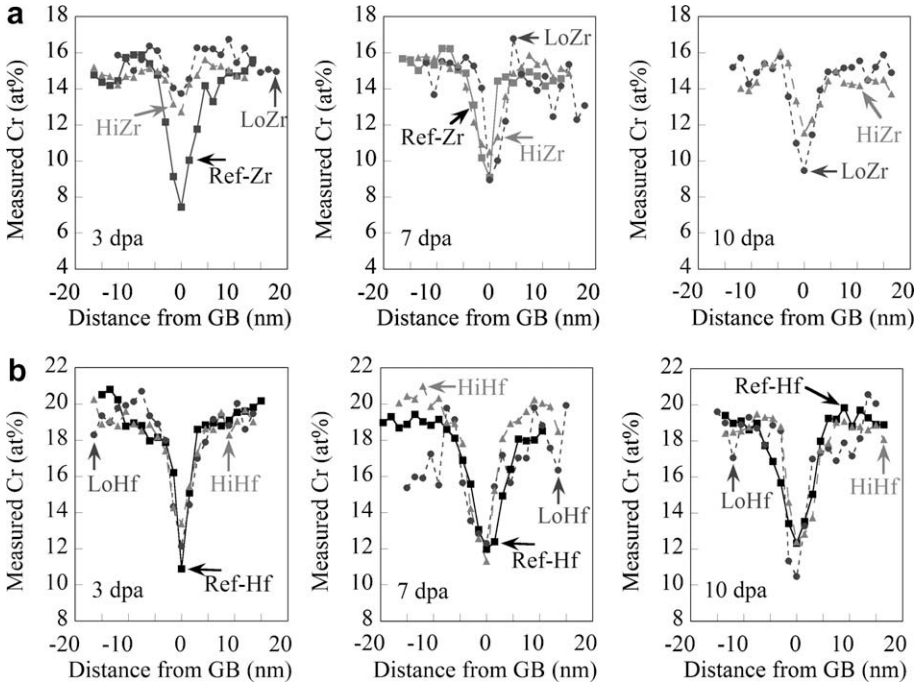

Fig. 1. Cr concentration profiles as a function of distance from the grain boundary at 400 °C for (a) Ref-Zr, LoZr and HiZr, and for (b) Ref-Hf, LoHf and HiHf, at doses of 3, 7 and 10 dpa.

with the trends in segregation for the +Zr and +Hf alloys at other doses. The inconsistency will be addressed more fully later.

By 10 dpa, the trend in segregation behavior is more similar to the behavior at 3 dpa. Cr depletion is again the lowest for the HiHf alloy. Cr depletion measured 6.9 at.% for Ref-Hf, 7.6 at.% for LoHf and 6.4 at.% for HiHf. Based on these segregation results, however, Hf addition clearly shows less of a change in Cr depletion at 3 dpa than Zr addition, and neither LoHf nor HiHf show any significant reduction in Cr depletion above 3 dpa.

3.1.2. RIS at 500 °C

All 500 °C RIS measurement values for the +Zr and +Hf alloys are given in Tables 4 and 5, respectively. The results are again normalized to Fe + Cr + Ni + Mn + Si + Zr = 1 for the +Zr alloys and normalized to Fe + Cr + Ni + Mn + Mo + Si = 1 for the +Hf alloys. The tables also provide segregation data renormalized to Fe + Cr + Ni = 1.

Measured Cr concentration profiles for the +Zr alloys at doses of 1 and 3 dpa are shown in Fig. 2(a) Similar profiles for the +Hf alloys are given in Fig. 2(b). A substantial difference exists between Ref-Zr and both LoZr and HiZr, at 1 dpa, where Cr depletion is 8.8 at.% for Ref-Zr, compared to just 4.7 at.% for LoZr and 3.6 at.% for HiZr. The Ref-Zr alloy has twice the amount of Cr depletion for LoZr and more than twice the amount for HiZr, showing that Zr addition again causes less Cr depletion.

The results at 3 dpa show that only HiZr has a measurable difference from Ref-Zr, with 8.2 at.% Cr depletion for Ref-Zr and 5.5 at.% for HiZr. Meanwhile, LoZr had slightly more Cr depletion than the reference alloy at 9.7 at.%.

Table 4
Grain boundary concentration measurements for the +Zr alloys irradiated with protons at 500 °C to doses of 1 and 3 dpa.

Alloy	Dose (dpa)	# of GB's	# of profile meas.		Measured concentration (at.%), normalized to 1						Segregation (at.%), renormalized		
					Fe	Cr	Ni	Mn	Si	Zr	Fe	Cr	Ni
Ref-Zr	1	2	6	GB	60.7 ± 1.4	6.5 ± 0.2	30.1 ± 1.3	0.73 ± 0.07	1.93 ± 0.98	–	−8.9 ± 1.6	−9.0 ± 0.6	17.8 ± 1.4
				Matrix	69.8 ± 0.7	15.4 ± 0.6	12.8 ± 0.4	1.25 ± 0.21	0.85 ± 0.33	–			
	3	2	6	GB	56.9 ± 1.7	7.2 ± 0.3	33.6 ± 1.6	0.69 ± 0.13	1.57 ± 0.24	–	−13.0 ± 1.6	−8.3 ± 0.6	21.3 ± 1.4
				Matrix	69.8 ± 0.9	15.4 ± 0.4	12.8 ± 0.7	1.25 ± 0.17	0.76 ± 0.10	–			
LoZr	1	2	7	GB	58.1 ± 1.8	10.7 ± 0.7	27.7 ± 1.4	1.78 ± 0.62	1.44 ± 0.31	NM	−10.5 ± 2.0	−4.7 ± 1.0	15.2 ± 1.9
				Matrix	68.9 ± 0.8	15.4 ± 0.7	13.2 ± 1.2	1.53 ± 0.43	0.77 ± 0.12	NM			
	3	2	10	GB	55.5 ± 1.2	5.7 ± 0.5	35.0 ± 2.4	0.64 ± 0.05	2.81 ± 0.35	NM	−13.5 ± 1.5	−9.8 ± 0.8	23.3 ± 2.4
				Matrix	69.5 ± 0.9	15.4 ± 0.7	12.8 ± 0.3	1.32 ± 0.05	0.77 ± 0.13	NM			
HiZr	1	2	13	GB	62.2 ± 2.4	11.4 ± 0.7	23.5 ± 1.7	1.07 ± 0.09	1.29 ± 0.46	0.52 ± 0.12	−7.4 ± 2.8	−3.6 ± 0.9	11.0 ± 2.0
				Matrix	69.8 ± 1.4	15.0 ± 0.5	12.9 ± 1.0	1.22 ± 0.19	0.81 ± 0.20	NM			
	3	2	12	GB	64.7 ± 2.0	9.4 ± 0.4	22.4 ± 2.4	0.67 ± 0.11	2.37 ± 0.68	0.49 ± 0.28	−4.6 ± 2.0	−5.5 ± 0.4	10.1 ± 2.4
				Matrix	70.0 ± 0.4	14.9 ± 0.1	12.8 ± 0.3	1.19 ± 0.03	0.83 ± 0.21	NM			

NM: Not Measurable.

Table 5
Grain boundary concentration measurements for the +Hf alloys irradiated with protons at 500 °C to doses of 1 and 3 dpa.

Alloy	Dose (dpa)	# of GB's	# of profile measured		Measured concentration (at.%), normalized to 1						Segregation (at.%), renormalized		
					Fe	Cr	Ni	Mn	Mo	Si	Fe	Cr	Ni
Ref-Hf	3	2	6	GB	56.9 ± 2.1	8.6 ± 0.6	32.7 ± 2.5	0.58 ± 0.10	0.65 ± 0.05	0.51 ± 0.10	−8.8 ± 2.2	−10.9 ± 1.0	19.6 ± 2.6
				Matrix	64.9 ± 0.6	19.1 ± 0.8	13.4 ± 0.8	1.05 ± 0.12	1.32 ± 0.12	0.24 ± 0.02			
LoHf	1	2	7	GB	60.8 ± 0.4	12.8 ± 0.3	24.2 ± 0.8	0.69 ± 0.02	1.05 ± 0.04	0.45 ± 0.08	−5.4 ± 0.8	−6.2 ± 0.5	11.6 ± 0.8
				Matrix	65.8 ± 0.7	18.8 ± 0.4	12.8 ± 0.3	1.05 ± 0.15	1.28 ± 0.13	0.28 ± 0.02			
	3	2	10	GB	56.6 ± 2.0	8.7 ± 0.6	33.1 ± 2.2	0.49 ± 0.23	0.58 ± 0.26	0.56 ± ± 0.27	−10.0 ± 2.0	−10.5 ± 0.6	20.4 ± 2.2
				Matrix	65.8 ± 0.6	18.8 ± 0.5	12.9 ± 0.5	1.05 ± 0.13	1.28 ± 0.10	0.28 ± 0.03			
HiHf	1	2	13	GB	61.8 ± 0.5	13.8 ± 0.2	22.2 ± 0.7	0.84 ± 0.09	1.10 ± 0.12	0.27 ± 0.03	−4.4 ± 0.8	−4.9 ± 0.6	9.3 ± 0.8
				Matrix	65.8 ± 0.6	18.5 ± 0.5	13.1 ± 0.3	1.09 ± 0.23	1.29 ± 0.08	0.20 ± 0.02			
	3	2	12	GB	54.5 ± 2.8	8.1 ± 0.3	36.2 ± 2.9	0.44 ± 0.10	0.55 ± 0.04	0.25 ± 0.04	−12.3 ± 2.9	−10.8 ± 0.3	23.1 ± 2.9
				Matrix	65.8 ± 0.5	18.6 ± 0.1	13.1 ± 0.4	1.04 ± 0.03	1.29 ± 0.02	0.21 ± 0.06			

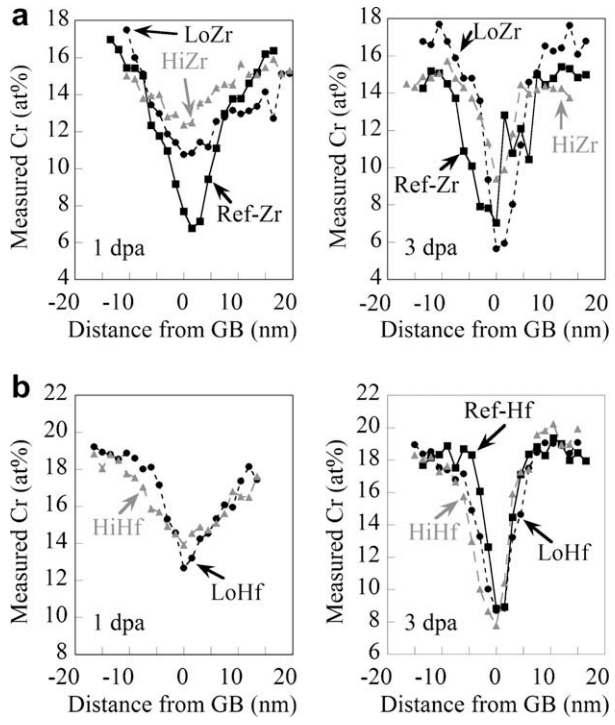

Fig. 2. Cr concentration profiles as a function of distance from the grain boundary at 500 °C for (a) Ref-Zr, LoZr and HiZr, and for (b) Ref-Hf, LoHf, and HiHf, at doses of 1 and 3 dpa.

Segregation was not measured for Ref-Hf at 1 dpa. Based on the results for Ref-Zr, for which Cr depletion is slightly higher at 1 dpa than at 3 dpa, it is expected that RIS will not change much between 1 and 3 dpa for the Ref-Hf alloy either. For the 1 dpa data, Cr depletion is 6.0 at.% for LoHf and 4.7 at.% for HiHf. Given that Cr depletion for Ref-Hf is 10.5 at.% at 3 dpa, these results would indicate some difference between the +Hf alloys and Ref-Hf at 1 dpa. By 3 dpa, the Cr depletion results are virtually identical for all three of the +Hf alloys. Ref-Hf, as mentioned, measures 10.5 at.% Cr depletion, with 10.1 at.% and 10.5 at.% for LoHf and HiHf, respectively. The 500 °C, 3 dpa Cr depletion values show no difference in RIS for the +Hf alloys.

3.2. Dislocation loops and precipitates

The dislocation loop microstructure of the irradiated alloys is examined at doses of 3 and 7 dpa at 400 °C. The temperature and doses were chosen in order to examine changes in the loop microstructure over the range in which RIS changes dramatically. The examination allows a broader assessment of the effects of oversized solutes on point defect trapping, where enhanced recombination should both reduce RIS and decrease the loop size and/or density.

Dark-field loop images are shown in Fig. 3 which are representative of the +Zr and +Hf alloys at 3 and 7 dpa. The scale marker shown for Ref-Zr at 3 dpa is the same for all images. The results of measurements of the average loop diameter and average loop density with standard deviation are listed in Table 6. No significant differences exist among the alloys for the average loop diameter at either 3 or 7 dpa, indicating saturation of the loop microstructure by 3 dpa. Diameters for the +Zr alloys at 3 range from 8.0 to 10.0 nm, with no change in diameter at 7 dpa, with sizes between

8.0 and 9.9 nm. Among the +Hf alloys, there are no significant differences in loop size, with diameters of 9.4, 7.2 and 7.2 nm for Ref-Hf, LoHf and HiHf, respectively. The range of diameters at 7 dpa is 8.9–10.4 nm.

Although the measured loop diameters are all relatively similar amongst the alloys, significant differences exist in the loop densities. At 3 dpa, the loop density for Ref-Zr is at least a factor of five higher than that for LoZr or HiZr, measuring 5.06×10^{22} m^{-3} for Ref-Zr compared to 1.08×10^{22} m^{-3} for LoZr and 8.73×10^{21} m^{-3} for HiZr. By 7 dpa in Ref-Zr, there was little change in loop density whereas the densities for LoZr and HiZr increased by 50–60%.

Average loop densities for the +Hf alloys also have large differences at 3 dpa, with a 40% decrease in loop density for LoHf and a 70% decrease for HiHf compared to Ref-Hf. By 7 dpa, the loop densities for LoHf and HiHf increased by as much as 50%, whereas the density for Ref-Hf remained unchanged.

The total loop line length is an aggregate measure of the total dislocation loop population in the microstructure. The loop line length is a combination of the average loop circumference times the dislocation density, with units of m^{-2}. Loop line lengths were fairly constant from 3 to 7 dpa for Ref-Zr and Ref-Hf. Meanwhile, loop line lengths for LoZr and HiZr increased by 60% or more from 3 to 7 dpa, and LoHf and HiHf more than double in value between the same doses. Loop line length results are also shown in Table 6.

An estimate of the average precipitate size and density in the oversized solute alloys was obtained by TEM imaging of the LoZr,

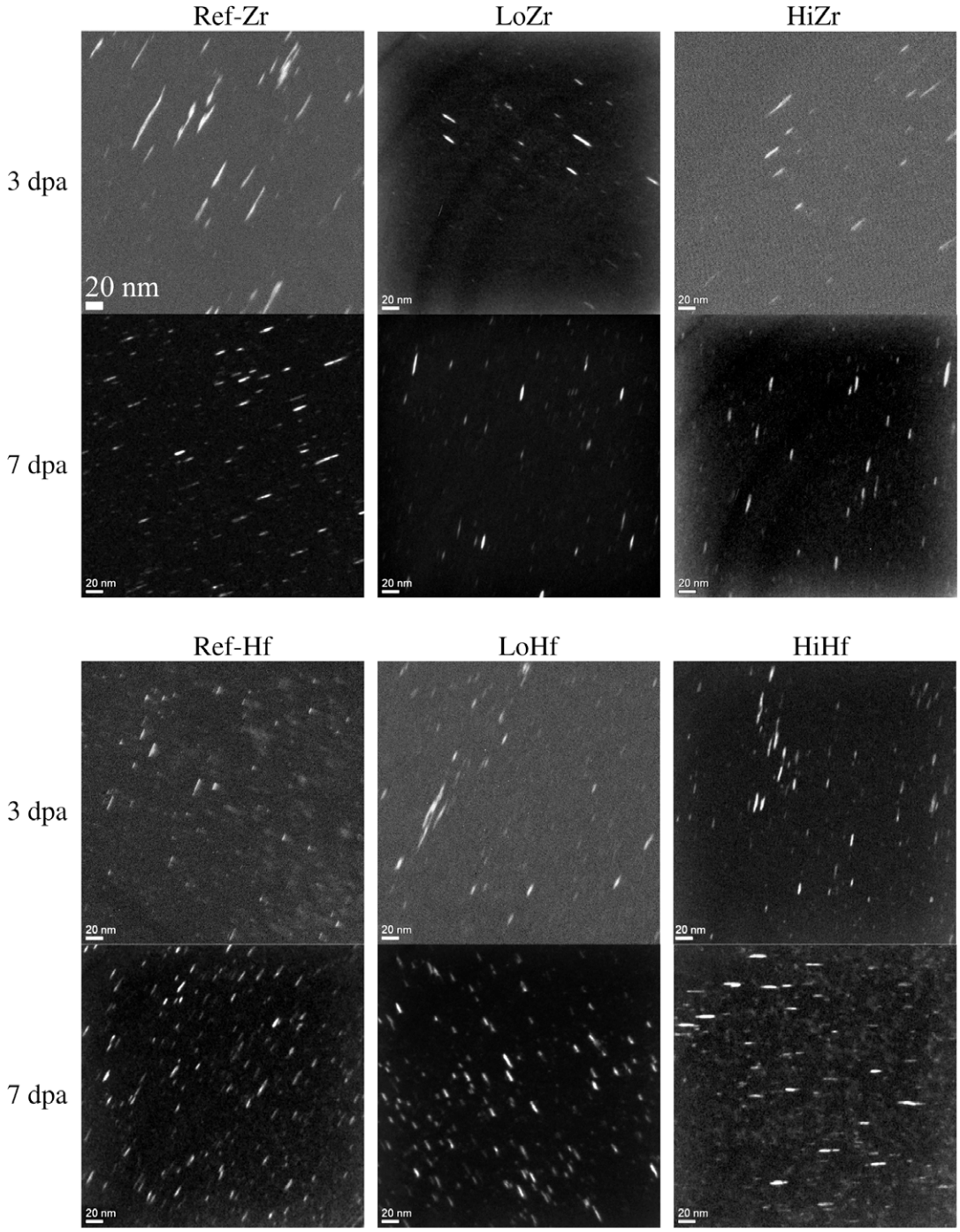

Fig. 3. Dislocation loop images for the +Zr and Hf alloys irradiated with protons at 400 °C to doses of 3 and 7 dpa.

Table 6
Measured dislocation loop data for the +Zr and +Hf alloys after 400 °C irradiation at doses of 3 and 7 dpa.

Alloy	Dose (dpa)	# of loops measured	Average loop diameter (nm)	Average loop density $\times 10^{21}$ (m^{-3})	Loop density uncertainty (%)	Total loop line length (m^{-2})
Ref-Zr	3	88	10.0	50.6×10^{21}	19.3	15.9×10^{14}
	7	303	8.7	54.8×10^{21}	8.2	14.9×10^{14}
LoZr	3	77	8.0	11.1×10^{21}	20.1	2.72×10^{14}
	7	318	8.0	17.2×10^{21}	11.6	4.35×10^{14}
HiZr	3	59	9.0	8.73×10^{21}	32.3	2.47×10^{14}
	7	282	9.9	13.2×10^{21}	21.1	4.1×10^{14}
Ref-Hf	3	388	9.4	22.9×10^{21}	15.6	6.74×10^{14}
	7	208	9.6	23.2×10^{21}	17.3	7.03×10^{14}
LoHf	3	124	7.2	13.8×10^{21}	15.9	3.11×10^{14}
	7	289	8.9	23.8×10^{21}	10.6	6.64×10^{14}
HiHf	3	42	7.2	6.32×10^{21}	6.8	1.43×10^{14}
	7	87	10.4	9.32×10^{21}	12.4	3.05×10^{14}

Table 7
Mean size and density of HfC and ZrC precipitates (ppts.) in HiHf and HiZr, respectively, with the amount of Hf/Zr in the precipitates and remaining in solution.

Alloy	Average size (nm)	Average density (m^{-3})	Density uncertainty (m^{-3})	Estimated solute in precipitates (at.%)	Estimated solute in solution (at.%)
HiHf	62 ± 36	7.0E + 19	±2.2E + 19	0.21	0.16
LoZr	81 ± 32	2.5E + 19	±1.1E + 19	0.17	0.11
HiZr	81 ± 32	2.5E + 19	±1.1E + 19	0.17	0.11

HiZr and HiHf alloys. LoZr has a precipitate density of 1.4×10^{19} m^{-3} and an average size of 84 ± 36 nm. HiZr has a density of 2.5×10^{19} m^{-3} with a mean size of 81 ± 32 nm. The density for HiHf is 7×10^{19} m^{-3} and the mean size is 62 ± 36 nm. The uncertainties are one standard deviation of the measurements. Based on the average precipitate size and density, the amount of solute still in solution was estimated at 0.09 at.% for LoZr, 0.11 at.% for HiZr, and 0.16 at.% for HiHf. Results of the precipitate measurements are summarized in Table 7.

In addition, Table 8 includes results from the APT analysis which will be further discussed in Section 4.3.2. The table lists whether or not oversized solute was detected in solution for that particular alloy condition and whether or not this led to a decrease in Cr depletion. So for example, the APTresults in the unirradiated condition would be expected to have an effect on the RIS results at 3 dpa, and APTresults for the 3 dpa irradiation condition should have an effect on the RIS results at 7 dpa. Additional details for the APTresults, including mass-to-charge spectra for the specimens analyzed, can be found in Ref. [11].

4. Discussion

The results from these experiments show trends that will be explained in this section. Comparison of the reference alloy RIS and loop data with literature data is made to ensure that reference alloy results are consistent with literature data and that differences in RIS and loop microstructure for the oversized solute alloys can be attributed to the solute additions. Model and experimental results are then compared to show that solute additions suppress RIS at low dose (3 dpa at 400 °C and 1 dpa at 500 °C). However, the results indicate that oversized solutes lose their effectiveness on suppressing RIS with increasing radiation dose, which may be due to two potential mechanisms, discussed more below. Both mechanisms are assessed, and analytical and empirical evidence is provided to suggest that solute-precipitate growth during irradiation is responsible for the loss of solute effect on RIS.

Table 8
Results from the identification of oversized solute in atom probe sample analysis.

Alloy	Oversized solute detected?	Subsequent Reduction in Cr depletion?	APT results consistent with RIS results?
LoZr	At 0 dpa, yes	By 3 dpa, yes	Yes
	At 3 dpa, no	By 7 dpa, no	Yes
	At 7 dpa, no	By 10 dpa, no	Yes
HiZr	At 0 dpa, yes	By 3 dpa, yes	Yes
	At 3 dpa, yes	By 7 dpa, yes	Yes
	At 3 dpa, yes	By 10 dpa, yes	Yes
LoHf	At 0 dpa, no	By 3 dpa, no	Yes
HiHf	At 0 dpa, yes	By 3 dpa, yes	Yes
	At 3 dpa, no	By 7 dpa, no	Yes

4.1. Reference alloy behavior

4.1.1. Radiation-induced segregation in the reference alloys

A comparison of RIS in the reference alloys to literature values is made against irradiation data for similar alloys under similar irradiation conditions to validate the measurements against other literature data. The 400 and 500 °C Cr depletion data from this study includes comparison with other proton irradiations and also neutron irradiations [1,2,15–21].

In Fig. 4, the amount of Cr depletion is plotted as the change from the bulk composition as a function of dose. For proton irradiations at 400 °C, the literature data show that the amount of Cr depletion increases quickly at low dose, followed by a gradual increase and saturation after 3 dpa to around 6–8 at.%. The Cr depletion in this study at 400 °C also falls in the range of 6–8 at.% and follows the same trend with dose. The 500 °C data from this study has more Cr depletion than at 400 °C by about 1.5 at.% for Ref-Zr and 3.5 at.% for Ref-Hf. Model calculations by Allen et al. [22] show that peak segregation occurred between 400 and 500 °C, and Damcott et al. [21] also measured slightly more Cr depletion at 500 °C than at 400 °C for Fe–20Cr–24Ni irradiated at 1 dpa. Assuming invariance of defects lost to sinks, neutron irradiation data from 275 to 288 °C [19,20,23] should be similar to proton irradiations at ~400 °C. At doses of 3 dpa or above, the amount of Cr depletion for the commercial purity alloys from Was et al. [16] and Asano et al. [19] is 5–9 at.%, which bounds the amount of Cr depletion measured for Ref-Zr and Ref-Hf at 400 °C from 3 to 10 dpa.

The amount of RIS for the reference alloys matches the expected trend as a function of dose at both 400 and 500 °C. RIS for the

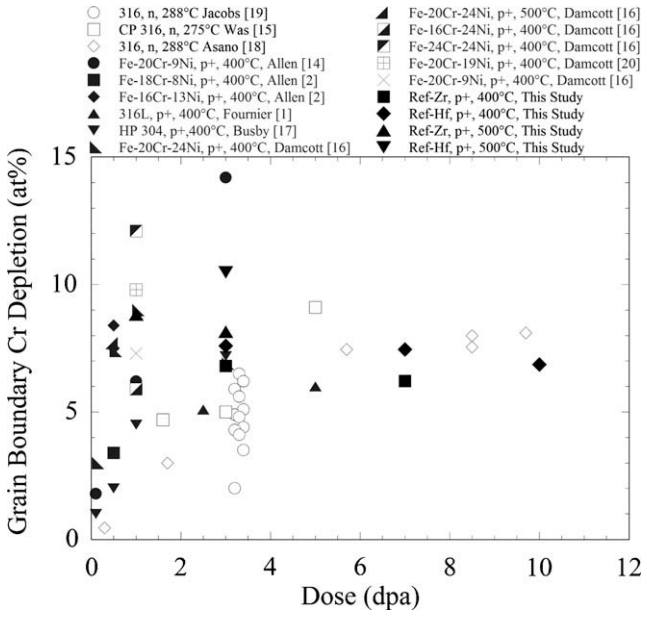

Fig. 4. A comparison of Cr depletion between the reference alloys in this study and literature values for neutron irradiation data (open symbols) and proton irradiation data (grey symbols), showing the amount of grain boundary (GB) Cr depletion as a function of dose for austenitic stainless steels at temperatures of 275–500 °C [1,2,15–17,19–21,43].

reference alloys is consistent with past literature results of similar alloys under similar irradiation conditions and provides a solid basis for comparison with the oversized solute alloys.

4.1.2. Experiment-model comparison of RIS

To provide further support for the validity of the RIS measurements, the reference alloy RIS measurements were compared to values calculated by the modified inverse-Kirkendall (MIK) model, which has been shown to predict RIS in austenitic alloys rather well [15,22,24]. The MIK model is a rate theory code based on the Perks model [25] but uses composition-dependent diffusivities for atoms and defects to calculate RIS for a ternary Fe–Cr–Ni alloy. Both calculated and experimental values of grain boundary Cr depletion for the Ref-Zr and Ref-Hf alloys at 400 °C are shown in Fig. 5. Model calculations are shown with cross-hatch bars, and measurements with solid bars. These patterns for model and experiment will be used throughout. Ref-Zr is shown in light grey and Ref-Hf in dark grey, with the error bars representing one standard deviation of the measurement. Model values for Ref-Zr and Ref-Hf differ slightly because of their differences in composition. Note that Ref-Zr is not measured at 10 dpa.

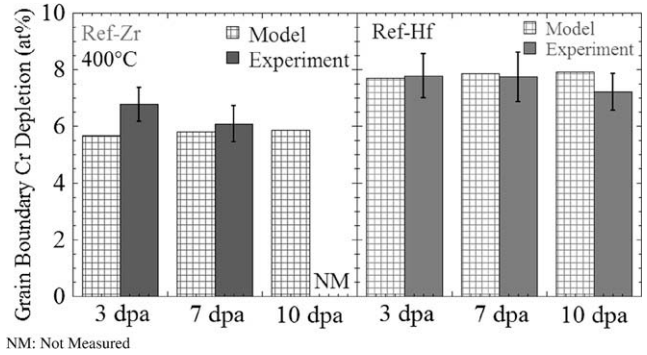

Fig. 5. A comparison for Ref-Zr and Ref-Hf of the MIK model and experimental measurements of grain boundary Cr depletion at 400 °C.

In all cases but one, Cr depletion measurements match the MIK model calculations within the uncertainties of the measurements. The only exception is Ref-Zr at 3 dpa, where the measured Cr depletion is 1 at.% greater than the calculated value. Generally, these results show good agreement between model and measurement for Cr depletion. Also, the measured results are relatively constant as a function of dose, which fits the expected trend for the model between 3 and 10 dpa.

4.1.3. Reference alloy loop microstructure

A comparison of average dislocation loop diameter as a function of dose is made with literature data for proton irradiations at 360 and 400 °C and neutron irradiation data from 275 to 400 °C [9,13,16,23,26–31]. The comparison between literature data and the reference alloys in this study irradiated at 400 °C is shown in Fig. 6(a). As the net flux of defects to sinks (loops) must remain invariant, the effect of neutron irradiations at 340 °C is similar to the effect of proton irradiation at ~380 °C [11]. The reference alloy loop diameters compare well with neutron irradiation data from 320 to 340 °C and are smaller than that for 400 °C neutron irradiation data [30], which is consistent with the effects of a higher temperature [30]. Meanwhile, reference alloy loop diameters are similar to other commercial purity alloys irradiated with protons at 400 °C [27].

Average loop densities for Ref-Zr and Ref-Hf are also compared against literature data, for proton and neutron irradiations [9,16,23,26–28]. The average loop densities as a function of dose is shown in Fig. 6(b). Neutron irradiation data at 320–340 °C, which compares to protons at 355–380 °C, most closely resembles the reference alloy data with a loop density about twice that of Ref-Zr at 7 dpa. Neutron irradiation loop densities at 275 °C are significantly higher than for proton irradiations at 400 °C and neutron irradiation loop densities at 400 °C are significantly lower than for proton irradiations at 400 °C which is consistent with the effect of temperature [11].

Loop diameters for Ref-Zr and Ref-Hf compare well with one another, and loop densities are higher for Ref-Zr compared to Ref-Hf due to the increase in Si concentration, which enhances the nucleation of dislocations [32–34]. The reference alloys have loop microstructures that are similar to 400 °C proton irradiation data for commercial alloys and neutron irradiation data from 320 to 340 °C. More importantly, the loop microstructure data for the reference alloys can be used in a comparative fashion to understand the effects of oversized solute additions on irradiated loop microstructure.

4.1.4. Relationship between loop microstructure and RIS

Loop densities saturated by 3 dpa for the reference alloys, but they had not saturated for the oversized solute alloys by 3 dpa. In fact, for LoZr, HiZr and HiHf, the loop densities are still below the values for the reference alloys by 7 dpa. Although uncertainties for the loop density measurements are significant, ranging from 6 to 32% of the measured values, the uncertainties are still well below the differences in loop density between the oversized solute and reference alloys, particularly at 3 dpa. The loop microstructure results provide further evidence for the effects of oversized solute additions in decreasing radiation damage.

Since the effect of oversized solute is to decrease the flux of defects at sinks by enhancing recombination, the effects of oversized solutes on RIS should be consistent with the effect on defect microstructure. A comparison is made between the amount of Cr depletion and the total loop line length, which is a product of the average loop circumference and density. A decrease in Cr depletion should correspond to a lower loop line length. The loop line length as a function of grain boundary Cr depletion is shown in Fig. 7. A direct relationship between the amount of grain boundary Cr

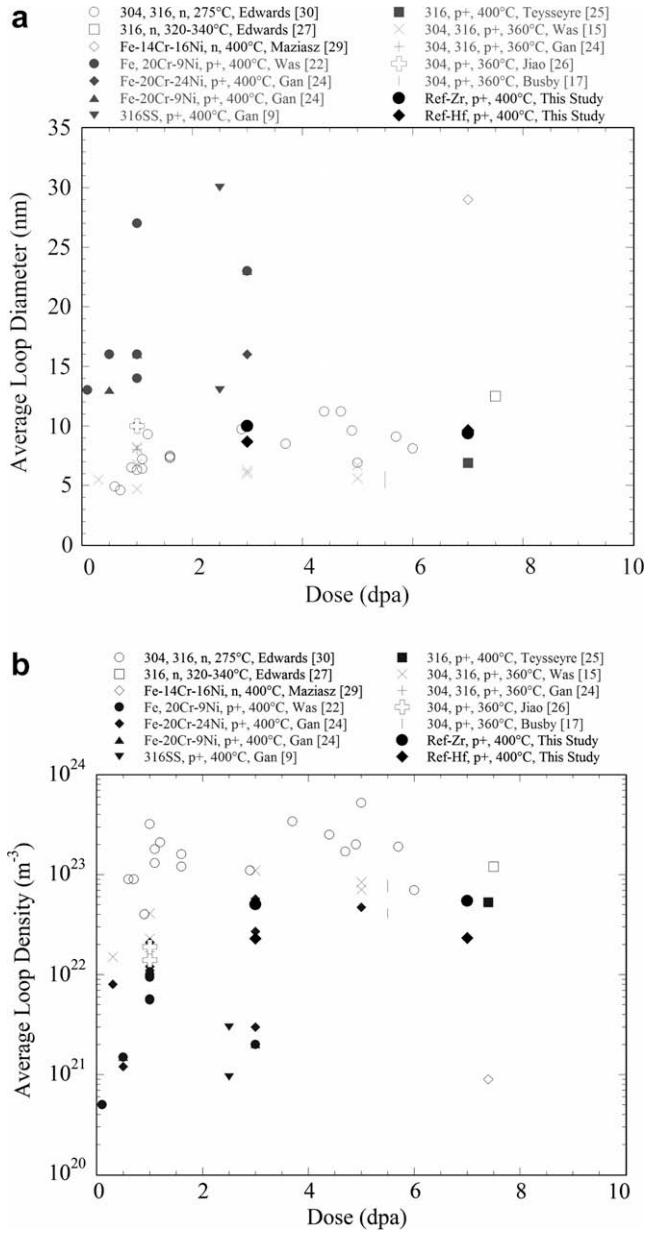

Fig. 6. Average loop (a) diameters and (b) densities for the reference alloys in this study compared to literature values for 316-type stainless steels irradiated with protons (grey symbols) and neutrons (open symbols) at temperatures of 275–400 °C [9,13,16,18,23,26–31].

depletion and the loop line length was observed. At 3 dpa, Ref-Zr has three times more Cr depletion and five times the total loop line length than for LoZr and HiZr. By 7 dpa, increases in the Cr depletion for LoZr and HiZr correspond to similar increases in the loop line length. The relationship between Cr depletion and loop line length is similar at 3 and 7 dpa, and illustrates how changes in the loop microstructure reflect changes in grain boundary RIS. The relationship is similar for the +Hf alloys at 3 dpa, where HiHf has the lowest amount of Cr depletion and the lowest loop line length. Meanwhile, the absence of oversized solute in the Ref-Hf alloy results in the highest amount of Cr depletion and loop line length.

The observations for loop line length and Cr depletion are consistent with a study by Gan et al. [9] who reported a substantial decrease in the loop line length compared to a reference 316SS after proton irradiation of the alloy heat as HiHf to 2.5 dpa at 400 °C.

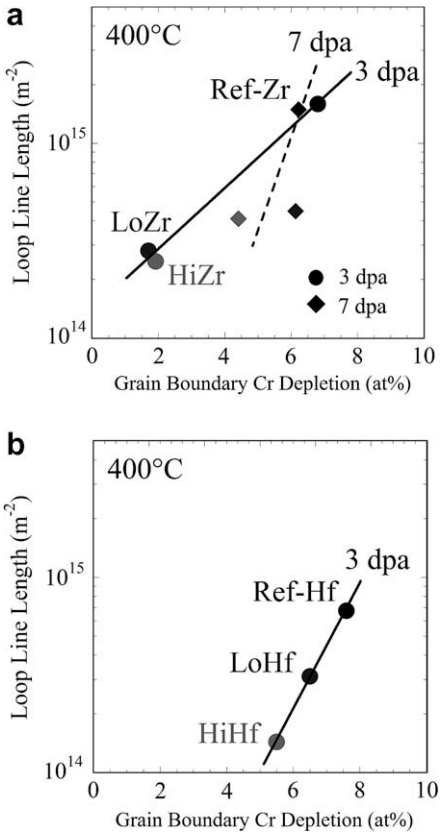

Fig. 7. Loop line length as a function of grain boundary Cr depletion for the (a) +Zr alloys at 3 and 7 dpa, 400 °C and for the (b) +Hf alloys at 3 dpa, 400 °C.

And Fournier et al. [1], in measuring the same irradiated specimens from Gan et al. [9], found substantially less Cr depletion for the +Hf alloy compared to their reference alloy. The work combined showed a simultaneous decrease in Cr depletion and loop line length with Hf addition to 316SS.

The loop microstructures of the irradiated oversized solute alloys are consistent with the RIS measurements in two ways: (1) at 400 °C and 3 dpa the suppression of loop nucleation and decrease in total loop line length corresponds to a decrease in RIS, and (2) increases in loop line lengths for the oversized solute alloys from 3 to 7 dpa are accompanied by similar increases in RIS. The loop microstructure data supports the vacancy trapping mechanism for oversized solutes by showing decreased defect concentrations through vacancy trapping and enhanced recombination.

4.2. Comparison of RIS measurement with model

Experimental segregation measurements for the +Zr and +Hf alloys are compared to the MIK model with trapping (MIK-T). The MIK-T model, described fully in Ref. [35], includes the effects of oversized solutes on RIS behavior. A comparison between experiment and model results provides an indication of whether the vacancy trapping mechanism can adequately describe the observed behavior. The oversized solute concentrations of the alloys were used as input to the MIK-T model with the assumption that all of the solute remained in solution.

Comparisons between model and experiment at 400 °C were made at a low (3 dpa) and high (7 dpa) dose. Since no 10 dpa data existed for Ref-Zr, the comparison is made at 3 and 7 dpa. A comparison for the +Hf alloys is made at 3 and 10 dpa and does not include 7-dpa data because the trend is not consistent with the data for either +Hf or +Zr alloys at any other dose or temperature, where

the reference alloy shows the most segregation while the alloy with highest solute concentration shows the least amount of segregation. Only at 7 dpa for HiHf is the trend different, with HiHf having more segregation than Ref-Hf or LoHf, yet a detailed review of the experiments showed no reason to suspect the data to be incorrect. As the measurements for HiHf at 7 dpa are not consistent with the other data, comparisons between model and experiment for the +Hf alloys will not rely on the 7 dpa irradiation condition.

The accurate prediction of Cr depletion is an important aspect of RIS modeling, so the focus will be on comparing experimental and calculated values for Cr depletion. For every alloy condition reported here, the trends in Ni and Si enrichment are the same as the trend for Cr depletion. The comparison between the MIK-T model and experimental measurements is sufficient to understand the behavior of oversized solutes on RIS and to assess the results.

The amount of Cr depletion between model and experiment at 400 °C and 3 dpa is shown in Fig. 8. The left side of the figure is for the +Zr alloys and the right side of the figure is for the +Hf alloys. The most striking feature is that the model predicts a significant reduction in Cr depletion for LoZr and HiZr relative to Ref-Zr, and the RIS measurements are consistent with the model. The model predicts a less significant reduction in Cr depletion for LoHf and HiHf compared to Ref-Hf, and measurements or LoHf and HiHf also show a reduction in Cr depletion. Though the reduction is less than predicted by the model, it is consistent with the trend of less Cr depletion for the +Hf alloys as compared to the +Zr alloys.

From Ref. [35], *ab initio* calculations had determined that the solute-vacancy binding energy for Zr, at 1.08 eV, is larger than for Hf, at 0.71 eV, meaning that Zr should be more effective in suppressing RIS than Hf. Thus, the MIK-T model predicts a larger reduction in RIS for Zr as compared to Hf. Segregation measurements confirm the calculated difference in solute-vacancy binding energies between Zr and Hf by showing a more significant reduction in Cr depletion for the +Zr alloys compared to the +Hf alloys at 400 °C and 3 dpa.

A comparison between model and experiment at 400 °C and 7 dpa for the +Zr alloys and 10 dpa for the +Hf alloys is shown in Fig. 9. The model predicts significant reduction of Cr depletion for LoZr and HiZr compared to Ref-Zr, and again for LoHf and HiHf compared to Ref-Hf. The measured values, however, no longer show a reduction in Cr depletion for the oversized solute alloys. LoZr and HiZr now more closely resemble the amount of Cr depletion for Ref-Zr, where only HiZr has a statistically significant difference in Cr depletion from Ref-Zr. Measurements for LoHf and HiHf have no statistically-significant difference from Ref-Hf, indicating no effect of Hf at the higher dose. One explanation for the lack of agreement at higher doses between model and experiment is that oversized solutes lose their effectiveness in reducing segregation at the higher dose.

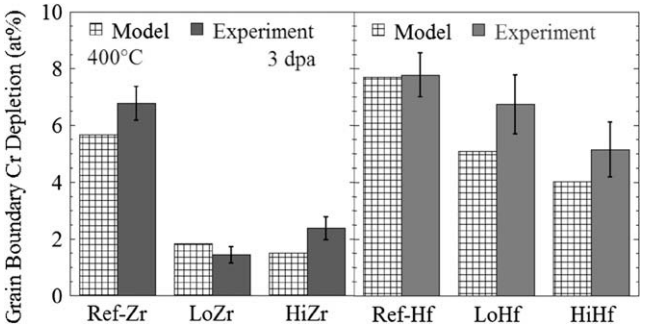

Fig. 8. Comparison of MIK-T and measured values of GB Cr depletion for the +Zr and +Hf alloys irradiated at 400 °C to 3 dpa.

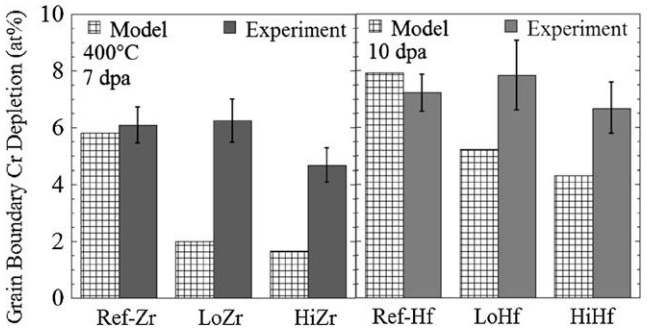

Fig. 9. Comparison of MIK-T and measured values of GB Cr depletion for the +Zr alloys irradiated at 400 °C to 7 dpa and +Hf alloys to 10 dpa.

The loss of solute effectiveness was observed by Fournier et al. [1] for 316SS with Hf, the same alloy heat as HiHf in this study, irradiated to doses of 2.5 and 5 dpa at 400 °C. At 2.5 dpa, Cr depletion was suppressed for the +Hf alloy relative to the reference alloy, with a difference of more than 3 at.%. By 5 dpa, Hf addition shows little benefit in reducing RIS, with a difference in Cr depletion of less than 1 at.% from the reference, similar to the difference in this study between Ref-Hf and HiHf at 10 dpa.

A comparison between model and experiment for the +Zr and +Hf alloys at 500 °C and 1 dpa is made in Fig. 10. The model predicts almost complete suppression of Cr depletion for LoZr and HiZr and calculates a large reduction in Cr depletion for LoHf and HiHf compared to Ref-Hf. Even though the values between model and experiment do not agree, the trend of the model is qualitatively consistent with experiments in showing a reduction in Cr depletion. In addition, LoZr and HiZr show less Cr depletion than LoHf and HiHf, which is consistent with Zr being more effective than Hf in reducing RIS.

Finally, model and experiment are compared for the oversized solute alloys at 500 °C and 3 dpa in Fig. 11. The model continues to show suppression of RIS for all of the oversized solute alloys. At 3 dpa, only HiZr still shows a reduction in Cr depletion relative to Ref-Zr, and the reduction is less than it was at 1 dpa. The measurements for LoZr, LoHf and HiHf show a similar amount of Cr depletion as their reference alloys, and the difference between model and experiment can again be explained by a loss of solute effectiveness on RIS at higher dose.

Segregation measurements confirm the difference in solute-vacancy binding energies between Zr and Hf determined by *ab initio* calculations. At all temperatures (400 and 500 °C) and at all doses studied from 1 to 10 dpa, any reduction in Cr depletion is greater for the +Zr alloys than for the +Hf alloys. As a result, RIS measure-

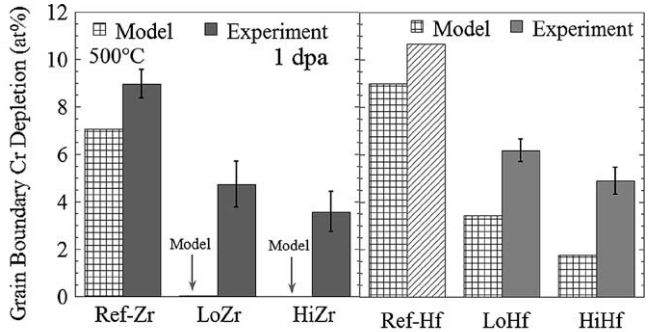

* Ref-Hf at 1 dpa was not measured. The value for Ref-Hf at 3 dpa serves as an estimate of the expected Cr depletion at 1 dpa.

Fig. 10. Comparison of MIK-T and measured values of GB Cr depletion for the +Zr and +Hf alloys irradiated at 500 °C to 1 dpa.

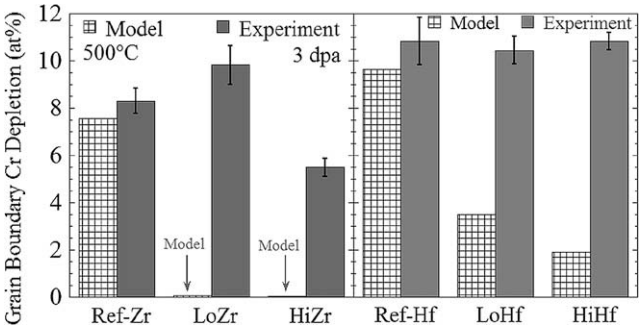

Fig. 11. Comparison of MIK-T and measured values of GB Cr depletion for the +Zr and +Hf alloys irradiated at 500 °C to 3 dpa.

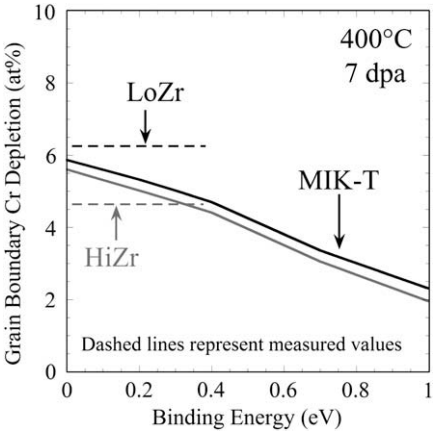

Fig. 12. Amount of GB Cr depletion at 400 °C for the +Zr alloys at 7 dpa compared to the MIK-T model as a function of binding energy.

ments confirm the results of first-principles calculations in showing a greater effectiveness of Zr relative to Hf on reducing RIS due to the larger binding energy for Zr at 1.08 eV relative to Hf at 0.71 eV.

4.3. Loss of oversized solute effectiveness

Measured reduction of Cr depletion disappears after 3 dpa at 400 °C and after 1 dpa at 500 °C for the +Zr and +Hf alloys, indicating that the effectiveness of oversized solute disappears more quickly as a function of dose at the higher temperature. Given that: (1) the behavior of RIS in the reference alloys was validated against literature data and also against model calculations, and (2) oversized solutes were only effective in suppressing Cr depletion at low doses, then the disappearance of the effect of oversized solutes on RIS with increasing dose must be due to changes in the irradiated microstructure. The loss of effect on RIS from oversized solutes could come from two sources: (1) solute poisoning, and (2) a loss of the oversized solute from the matrix.

4.3.1. Solute poisoning

Solute poisoning may occur when the oversized solute atom is nearest neighbors with small substitutional atoms, decreasing an oversized solute atom's ability to trap vacancy defects and enhance recombination. The decreased recombination would in turn cause a loss of effect on RIS. Since vacancy trapping enhances recombination with interstitials, smaller substitutional atoms, like Si, migrating as interstitials, could recombine with the vacancy to become first nearest neighbors of the oversized solute atom. Alternatively, a small interstitial could bind with the vacancy. In either case, the effect would be a reduction in the strain field surrounding the oversized solute atom or a change in electronic effects with neighboring atoms. The effects of solute poisoning could take two forms: (1) a decrease in the trapping and recombination radii, or (2) a decrease in the solute-vacancy binding energy.

The trapping and recombination radii define the interaction volume around the solute atom. Since the MIK-T model was shown in Ref. [35] to be relatively insensitive to both variables, decreasing the interaction volumes would have virtually no effect on segregation, so decreasing the trapping or recombination radii is unlikely to be the cause for the loss of effect from oversized solutes on RIS.

Solute poisoning could also reduce the binding energy of oversized solute atoms by decreasing the elastic interaction energy between the vacancy and solute atom. No *ab initio* calculations were performed to quantify this effect, but in Fig. 12, grain boundary Cr depletion for the +Zr alloys irradiated to 7dpa at 400 °C is shown for the MIK-T model as a function of binding energy from 0 to 1 eV. The dashed lines represent the measured Cr depletion values for the alloys. For LoZr, the measured value is greater than any of the calculated values and best matches the model at 0 eV. For HiZr, agreement between model and experiment is at approximately 0.3 eV. Though not shown, agreement between model experiment for the +Hf alloys is similar to the +Zr alloys. Solute poisoning would therefore have to reduce binding energies to 0–0.3 eV for Zr and Hf.

No experimental measurements or calculations exist that can be used to substantiate the reduction in binding energy for Zr or Hf. Such a large reduction in strain would include at least the relaxation from a trapped vacancy defect [11,36]. Since the reduction in binding energy requires the trapping of a vacancy, it contributes to the mechanism of enhanced recombination. The end result is that solute poisoning is not able to explain the loss of solute effectiveness on RIS.

4.3.2. Oversized solute precipitation

A second possible explanation for the loss of solute effectiveness on RIS is that the solute is lost from solution due to a precipitation reaction. The question then is whether or not solute can be lost to precipitates during proton irradiations. At temperatures of 500 and 600 °C, Ohnuki et al. [37] did observe a high density of fine ZrC or HfC precipitates in 316SS that developed after neutron irradiation. Although precipitates were observed both before and after irradiation in the oversized solute alloys, precipitate growth during irradiation could not be confirmed by measuring a change in precipitate size. A complete loss of 0.37 at.% Hf in the HiHf alloy would give a precipitate size of 76 nm. Since the initial size was 62 ± 36 nm, the difference in average size between a complete loss of solute, at 76 nm, and the initial size is less than the uncertainty of the measurement. The result is similar for both the LoZr and HiZr alloys, where a complete loss of solute results in an average precipitate size that is within the uncertainty for the initial size [11]. Consequently, TEM imaging of precipitate size after irradiation cannot confirm precipitate growth from the loss of solute.

APT measurements of the oversized solute remaining in solution could, in this study, qualitatively confirm the loss of solute during irradiation. Measurements included each of the oversized solute alloys in the unirradiated condition in addition to measurements of irradiated samples of LoZr, HiZr, and HiHf. None of the specimens analyzed contained a ZrC or HfC precipitate in the sample volume; therefore, any Zr or Hf detected in the mass/charge spectra were attributed to the in-solution concentration. For LoHf, Hf is not observed above the detection limit in the unirradiated condition, whereas Hf is detected in the HiHf alloy, and this corresponds to a small reduction in Cr depletion at 3 dpa. At 3 dpa, no Hf is detected in the HiHf alloy, and no reduction in Cr depletion is measured at 7 dpa. For LoZr, Zr is detected in the unirradiated

alloy, corresponding to a reduction in Cr depletion at 3 dpa, but Zr cannot be confirmed at 3 or 7 dpa and the reduction in Cr depletion disappears at higher dose. Only the HiZr alloy shows a statistically significant reduction in Cr depletion from the reference alloy at 7 dpa, and HiZr is also the only alloy to have confirmed oversized solute in solution at 3 and 7 dpa from APT analysis, showing that at least some measurable concentration of Zr has remained in solution.

The results of APT analysis and their correlation with RIS data are presented both in Table 8 and Fig. 14. Combined, the results answer the questions: (1) is any oversized solute remaining in solution according to APT, and (2) if so, does the alloy show a reduction in Cr depletion? For example, if oversized solute is confirmed by APT to be in solution at 0 dpa, then the oversized solute should suppress Cr depletion at 3 dpa. The results show that for every alloy condition measured by APT, there is consistency between the reduction in Cr depletion and the detection of solute in solution.

To estimate how much oversized solute must be lost in order for measured segregation to match the model calculations, the MIK-T model was run for oversized solute concentrations ranging between 0 and 0.1 at.%, shown in Fig. 13. The measured values of Cr depletion for the oversized solute alloys are shown by dashed lines. For HiZr, solute concentrations would need to be about 0.01 at.% at 7 dpa for the measurements to match the MIK-T model, where LoZr would require a complete loss of oversized solute from solution. Results for HiHf and LoHf, though not shown, are similar, requiring up to only 0.01 at.% of Hf remaining in solution for model results to match experimental measurements.

The loss of oversized solute in solution would require radiation-enhanced diffusion to existing precipitates. Work by Abraham et al. [38] has shown that for stainless steel with Zr, the solubility of Zr drops to zero at temperatures below 600 °C. Phase diagram calculations using FactSage [39] with the SGTE database (applicable to metals and alloys) support the lack of solubility for Zr and Hf. Consequently, the remaining Zr and Hf should be removed from solution during irradiation since the diffusion kinetics are increased due to higher point defect concentrations. The question is whether or not the diffusion process can occur on time scales of proton irradiations.

An analysis using precipitation kinetics developed by Shewmon [40] considers the loss of solute as a function of irradiation time. A complete description of the analysis is provided in Ref. [11]. The final solution determines the average solute concentration, $\bar{c}$, remaining in solution, according to the equation:

$$\bar{c} = c_0 - \left(\frac{2D(c_0 - c')t}{c_p^{\frac{1}{3}} r_e^2} \right)^{\frac{3}{2}}, \quad (1)$$

where c_0 is the initial solute concentration outside of the precipitate, D is the diffusion coefficient, c' is the matrix concentration in equilibrium with the precipitate, t is the irradiation time, c_p is the atom fraction of the solute in the precipitate and r_e is half the distance between precipitates.

Assuming the oversized solute atoms can migrate only via the vacancy flux, then diffusion coefficient, D, is described by:

$$D = D_v C_v, \quad (2)$$

where D is the product of the defect vacancy coefficient, D_v, and the vacancy concentration, C_v. Vacancy concentrations are the steady-state matrix concentrations taken from the MIK model, with vacancy atom fractions of $\sim 1.3 \times 10^{-6}$ at 400 °C and 2.0×10^{-7} at 500 °C, and the pre-exponential factor is taken from the pre-exponential factor for Cr in the MIK model at 4×10^{-6} m^2/s. The initial concentration of solute in the matrix, $c_{0,}$ prior to irradiation was estimated at 0.16 at.% for HiHf. Assuming that HfC precipitates are stoichiometric, then c_p is 0.5. For a precipitate density of 7×10^{19} m^{-3}, then $r_e = 1.21 \times 10^{-7}$ m. The remaining variable in the analysis is the migration energy for Zr or Hf, which in a Fe–Cr–Ni system is not known. The solution to Eq. (1) can be plotted as a function of migration energy to determine the value required for a complete loss of oversized solute in solution. Since the loss

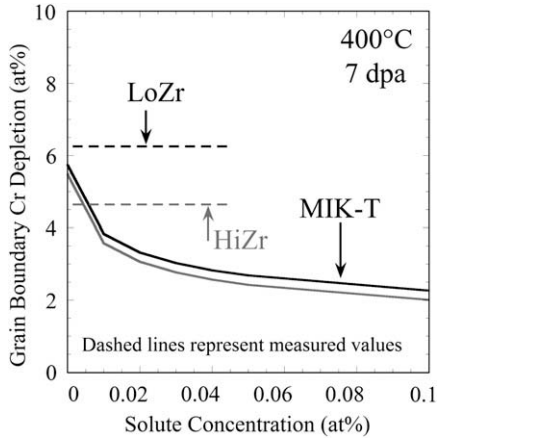

Fig. 13. Amount of GB Cr depletion as a function of solute concentration in solution for the +Zr alloys at 400 °C, 7 dpa. The binding energy is 1.08 eV for Zr.

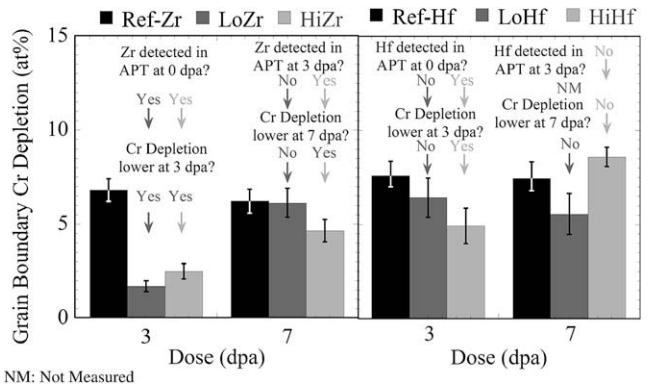

Fig. 14. Correlation of Cr depletion measurements and atom probe tomography analysis, where for each irradiation condition, the detection of oversized solute in solution is consistent with the measured reduction of Cr depletion.

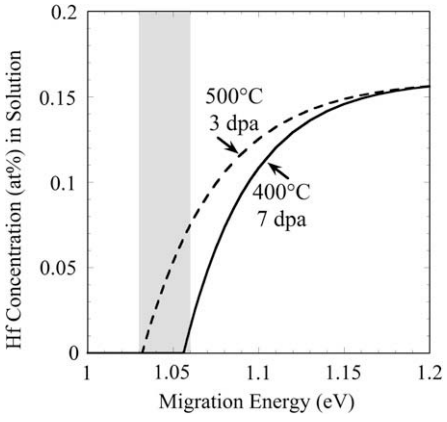

Fig. 15. Hf concentration remaining in solution as a function of migration energy at temperatures of 400 and 500 °C, based on the Cr vacancy diffusion coefficient, using a precipitation kinetics analysis developed by Shewmon [40].

of effectiveness on RIS is observed by 7 dpa at 400 °C and at 3 dpa at 500 °C, a fixed time at each temperature is used for the solution, where 1 dpa is $\sim 1.08 \times 10^5$ s.

The Hf concentration remaining in solution as a function of vacancy migration energy is shown in Fig. 15. The shaded region from 1.03 to 1.06 eV represents the values for which for the Hf concentration in solution is between 0 and 0.01 at.%, which matches the estimated solute in solution at 500 °C, 3 dpa and 400 °C, 7 dpa. Results for the analysis of LoZr and HiZr are similar, with a complete loss of solute from solution occurring with migration energies from 1.02 to 1.05 eV. Janotti et al. [41] addressed the diffusion of 4d and 5d transition elements in Ni and found that migration energies are lowest for Zr and Hf at around 0.2 eV, which is more than sufficient to explain the loss of solute from solution. Also, Krčmar et al. [42] and Janotti et al. [41], showed that larger solute atoms in fcc Ni diffuse faster through the vacancy flux than smaller solute atoms, and the vacancy migration energies for Zr and Hf from this analysis are less than the calculated vacancy migration energies of 1.16–1.18 eV for Fe, Cr and Ni in a similar alloy [16]. Finally, as shown in Fig. 15, the same migration energy for Hf can explain the loss of solute at 400 and 500 °C at the doses where a loss of solute effectiveness on RIS is observed.

The diffusion of oversized solutes to precipitates through the vacancy flux is not fully consistent with the trapping mechanism, since solute diffusion through vacancies may prevent them from acting as recombination centers. However, the processes for diffusion and recombination occur on very different time scales, with a trapped vacancy-interstitial recombination event requiring far less time than diffusion to a precipitate. For both Zr and Hf, the average lifetime of a vacancy-defect pair is on the order of 10^2–10^3 s, whereas diffusion to a precipitate requires time scales on the order of 10^7 s. Consequently the mobility of solute atoms is small relative to the time scales of vacancy trapping, recombination and release, with solute atoms remaining as trapping and recombination sites for most of their time in solution.

Previous comparisons of measured RIS with the MIK-T model used the oversized solute concentration of the bulk alloy. However, since some of the oversized solute was lost to precipitates prior to irradiation, using the estimated amount of solute remaining prior to irradiation should improve the correlation between model and experiment. The estimated solute concentration (0.11 at.% in HiZr and 0.16 at.% in HiHf) is used Fig. 16 to re-calculate Cr depletion at 400 °C. In Fig. 8, the MIK-T model values did not lie within the uncertainty of the measured values for HiZr or HiHf at 3 dpa. By using the estimated solute concentrations based on TEM imaging, the model values shown in Fig. 16 now lay within the uncertainties of the measured values for HiZr and HiHf at 400 °C and 3 dpa. The improved agreement between model and experiment confirms that an accurate value for the amount of solute in solution is important for understanding RIS behavior. Athe calculated and measured values for Cr depletion no longer agree at high dose, if the model included a further loss of solute due to precipitate growth at the higher dose, the model values may again be consistent with experimental measurements.

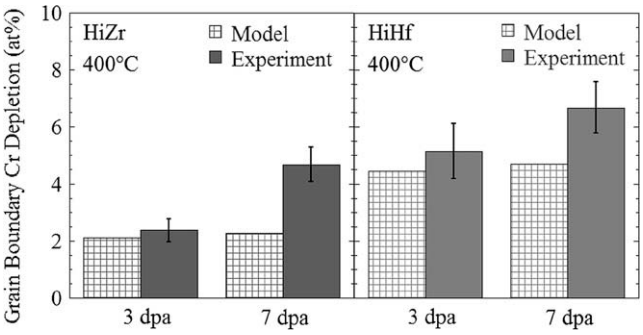

Fig. 16. Comparison of MIK-T model and measured values of GB Cr depletion at 400 °C for HiHZr and HiHf. Oversized solute concentrations for the MIK-T model are the estimated values prior to irradiation based on TEM imaging of ZrC and HfC precipitate microstructure, with 0.11 at.% Zr for HiZr and 0.16 at.% Hf for HiHf.

The significance of this analysis is that the removal of solute to precipitates by vacancy diffusion is possible under the conditions in these experiments. The estimated migration energy required to explain the loss of solute by precipitate growth is less than the Cr vacancy migration, which is consistent with the results of Janotti et al. [41] in showing lower migration energies for elements with a larger atomic radius such as Zr and Hf relative to Cr. And account accounting for the loss of oversized solute from solution due to precipitation results in better agreement between model-calculated RIS and measured values. As a result, the loss of solute by precipitate growth is the most likely mechanism to explain the loss of solute effectiveness on RIS.

5. Conclusions

Oversized solute atoms enhance point defect recombination through a solute-vacancy trapping mechanism, resulting in a reduction in grain boundary Cr depletion after proton irradiation to temperatures of 400 and 500 °C. However, Zr is observed to be more effective than Hf in reducing RIS because of the larger solute-vacancy binding energy for Zr. The experimental measurements are consistent with first principle calculations of solute-vacancy binding energy for Zr and Hf, and the MIK-T model agrees with RIS measurements in predicting greater effectiveness on RIS suppression by Zr compared to Hf. The effect of oversized solutes in reducing RIS disappears by 7 dpa at 400 °C and by 3 dpa at 500 °C. Since the MIK-T model predicts continued suppression of RIS, the difference between model and experiment indicates a change in the irradiated microstructure as the cause for the loss of solute effectiveness on RIS.

The loss of solute from solution is most likely due to diffusion to and incorporation into existing precipitates. Atom probe tomography measurements confirm a loss of oversized solute in solution with increasing dose. And the MIK-T model shows that almost a complete loss of solute is necessary to explain the behavior of RIS with increasing dose.

Acknowledgements

The authors would like to thank the staff of the Michigan Ion Beam Laboratory at the University of Michigan, including Victor Rotberg, Ovidiu Toader and Fabian Naab. The authors would also like to thank technical staff at Oak Ridge National Laboratory, including Jim Bentley, Ed Kenik, Neal Evans and Karren Moore. The authors are appreciative of scientific insight from colleagues at Lockheed Martin, including Reza Najafabadi and George Young. This research was supported by the US Department of Energy under grant DE-FG07-03ID14542. This research was also performed under appointment to the Naval Nuclear Propulsion Fellowship Program sponsored by Naval Reactors Division of the US DOE. A portion of this research was performed at the Oak Ridge National Laboratory SHaRE User Facility, sponsored by the Office of Basic Energy Sciences, US Department of Energy, under contract DE-AC05-00OR22725 with UT-Battelle, LLC.

References

[1] L. Fournier, B.H. Sencer, G.S. Was, E.P. Simonen, S.M. Bruemmer, J. Nucl. Mater. 321 (2003) 192.

[2] T.R. Allen, J.I. Cole, J. Gan, G.S. Was, R. Dropek, E.A. Kenik, J. Nucl. Mater. 342 (2005) 90.
[3] R.B. Dropek, G.S. Was, J. Gan, J.I. Cole, T.R. Allen, E.A. Kenik, Proceedings of the 11th International Conference on Environmental Degradation of Materials in Nuclear Power Systems – Water Reactors, American Nuclear Society, Stevenson, Washington, 2003.
[4] N. Sakaguchi, S. Watanabe, H. Takahashi, Nucl. Instrum. Meth. B 153 (1999) 142.
[5] S. Kasahara, K. Nakata, H. Takahashi, J. Nucl. Mater. 239 (1996) 194.
[6] T. Kato, H. Takahashi, M. Izumiya, J. Nucl. Mater. 189 (1992) 167.
[7] D.I.R. Norris, C. Baker, C. Taylor, J.M. Titchmarsh, in: R.E. Stoller, A.S. Kumar, D.S. Gelles (Eds.), Effects of Radiation on Materials: 15th International Symposium, ASTM STP 1125, ASTM, Philadelphia, PA, 1992, p. 603.
[8] F.A. Garner, H.R. Brager, J. Nucl. Mater. 155–157 (1988) 833.
[9] J. Gan, E.P. Simonen, S.M. Bruemmer, L. Fournier, B.H. Sencer, G.S. Was, J. Nucl. Mater. 325 (2004) 94.
[10] T. Allen, G. Was, S. Bruemmer, J. Gian, S. Ukai, Grant No. DE-FG07-03ID14542, Project No. 02-110, DOE, 2006.
[11] M.J. Hackett, Mechanism for Suppression of Radiation-Induced Segregation by Oversized Solute Addition in Austenitic Stainless Steel, University of Michigan, 2008.
[12] D.B. Williams, C.B. Carter, Transmission Electron Microscopy, Plenum Press, New York, NY, 1996.
[13] D.J. Edwards, E.P. Simonen, F.A. Garner, L.R. Greenwood, B.M. Oliver, S.M. Bruemmer, J. Nucl. Mater. 317 (2003) 32.
[14] M.K. Miller, K.F. Russell, Ultramicroscopy 107 (2007) 761.
[15] T.R. Allen, J.T. Busby, G.S. Was, E.A. Kenik, J. Nucl. Mater. 255 (1998) 44.
[16] G.S. Was, J.T. Busby, T.R. Allen, E.A. Kenik, A. Jenssen, S.M. Bruemmer, J. Gan, A.D. Edwards, P.M. Scott, P.L. Anderson, J. Nucl. Mater. 300 (2002) 198.
[17] D.L. Damcott, T.R. Allen, G.S. Was, J. Nucl. Mater. 225 (1995) 97.
[18] J.T. Busby, G.S. Was, E.A. Kenik, J. Nucl. Mater. 302 (2002) 20.
[19] K. Asano, K. Fukuya, K. Nakata, M. Kodoma, in: D. Cubicciotti (Ed.), Proceedings of the Fifth International Symposium on Environmental Degradation of Materials in Nuclear Power Systems – Water Reactors, American Nuclear Society, Monterey, CA, 1992, p. 838.
[20] A.J. Jacobs, G.P. Wozadlo, K. Nakata, S. Kasahara, T. Okada, S. Kawano, S. Suzuki, in: R.E. Gold, E.P. Simonen (Eds.), Proceedings of the Sixth International Symposium on Environmental Degradation of Materials in Nuclear Power Systems – Water Reactors, National Association of Corrosion Engineers, Houston, TX, 1993, p. 14.
[21] D.L. Damcott, The Use of Proton Irradiation in the Examination of Radiation-Induced Segregation in Multicomponent Alloys, University of Michigan, 1998.
[22] T.R. Allen, G.S. Was, Acta Mater. 46 (1998) 3679.
[23] G.S. Was, T.R. Allen, J.T. Busby, J. Gan, D. Damcott, D. Carter, M. Atzmon, E.A. Kenik, J. Nucl. Mater. 270 (1999) 96.
[24] T.R. Allen, Modeling of Radiation-Induced Segregation in Austenitic Fe–Cr–Ni Alloys, University of Michigan, 1998.
[25] J.M. Perks, S.M. Murphy, Materials for Nuclear Reactor Core Applications, BNES, London, 1987.
[26] J. Gan, G.S. Was, J. Nucl. Mater. 297 (2001) 161.
[27] S. Teysseyre, Z. Jiao, E. West, G.S. Was, J. Nucl. Mater. 371 (2007) 107.
[28] Z. Jiao, J.T. Busby, G.S. Was, J. Nucl. Mater. 361 (2007) 218.
[29] D.J. Edwards, E.P. Simonen, S.M. Bruemmer, J. Nucl. Mater. 317 (2003) 13.
[30] P.J. Maziasz, J. Nucl. Mater. 191–194 (1992) 701.
[31] D. Edwards, E. Simonen, S. Bruemmer, P. Efsing, in: 12th International Conference on Environmental Degradation of Materials in Nuclear Power Systems – Water Reactors, TMS, Salt Lake City, UT, 2005, p. 419.
[32] J. Cookson, R. Carter, D. Damcott, G.S. Was, M. Atzmon, J. Nucl. Mater. 202 (1993) 104.
[33] N. Shigenaka, T. Hashimoto, M. Fuse, J. Nucl. Mater. 207 (1993) 46.
[34] G.S. Was, J.T. Busby, EP-P3038/C1434, Electric Power Research Institute, 2002.
[35] M.J. Hackett, R. Najafabadi, G.S. Was, J. Nucl. Mater. 389 (2009) 279.
[36] T.L. Choy, Y.Y. Yeung, J. Phys. Chem. Solids 54 (1993) 553.
[37] S. Ohnuki, S. Yamashita, H. Takahashi, T. Kato, in: Effects of Radiation on Materials: 19th International Symposium, ASTM STP 1366, ASTM, West Conshochoken, PA, 2000, p. 756.
[38] D.P. Abraham, S.M. McDeavitt, J. Park, Metall. Mater. Trans. A 27 (1996) 2151.
[39] FactSage, Thermfact and GTT-Technologies, 5.5, 2007.
[40] Paul G. Shewmon, Diffusion in Solids, J. Williams Book Company, 1983.
[41] A. Janotti, M. Krčmar, C.L. Fu, R.C. Reed, Phys. Rev. Lett. 92 (2004) 085901.
[42] M. Krčmar, C.L. Fu, A. Janotti, R.C. Reed, Acta Mater. 53 (2005) 2369.
[43] J.T. Busby, Isolation of the Role of Radiation-Induced Segregation in Irradiation-Assisted Stress Corrosion Cracking in Proton-Irradiated Austenitic Stainless Steels, University of Michigan, 2001.